Article

Non-volatile electric-field control of inversion symmetry

Lucas Caretta [1,14,16] ✉, Yu-Tsun Shao[2,15,16], Jia Yu[3], Antonio B. Mei[4], Bastien F. Grosso [5], Cheng Dai[6], Piush Behera[1], Daehun Lee[3], Margaret McCarter[7], Eric Parsonnet [7], Harikrishnan K. P [2], Fei Xue[6], Xiangwei Guo [8,9], Edward S. Barnard [10], Steffen Ganschow[11], Zijian Hong [8], Archana Raja [10], Lane W. Martin [1,12], Long-Qing Chen [6], Manfred Fiebig [5], Keji Lai [3], Nicola A. Spaldin [5], David A. Muller [2,13], Darrell G. Schlom [4,11,13] & Ramamoorthy Ramesh [1,7,12] ✉

Competition between ground states at phase boundaries can lead to significant changes in properties under stimuli, particularly when these ground states have different crystal symmetries. A key challenge is to stabilize and control the coexistence of symmetry-distinct phases. Using $BiFeO_3$ layers confined between layers of dielectric $TbScO_3$ as a model system, we stabilize the mixed-phase coexistence of centrosymmetric and non-centrosymmetric $BiFeO_3$ phases at room temperature with antipolar, insulating and polar semiconducting behaviour, respectively. Application of orthogonal in-plane electric (polar) fields results in reversible non-volatile interconversion between the two phases, hence removing and introducing centrosymmetry. Counterintuitively, we find that an electric field 'erases' polarization, resulting from the anisotropy in octahedral tilts introduced by the interweaving $TbScO_3$ layers. Consequently, this interconversion between centrosymmetric and non-centrosymmetric phases generates changes in the non-linear optical response of over three orders of magnitude, resistivity of over five orders of magnitude and control of microscopic polar order. Our work establishes a platform for cross-functional devices that take advantage of changes in optical, electrical and ferroic responses, and demonstrates octahedral tilts as an important order parameter in materials interface design.

Crystal symmetry in condensed-matter materials largely dictates their micro- and macroscopic properties[1] and, in turn, their functionalities. Much effort has been devoted to designing and tuning symmetry in solid-state materials[2–8], with ferroelectrics being a particularly pervasive example of broken inversion symmetry[3] (Supplementary Fig. 1). For example, inversion symmetry in antiferroelectric materials can be broken by a strong electric field, converting the system into a volatile, field-stabilized polar phase[3]. Stabilization of competing low-energy ground states—for example, polar and antipolar phases—offer the

potential to interconvert between states with different crystallographic symmetries and order parameter–energy landscapes. Such competing phases are often realized by the growth of ferroelectric superlattices using layer-by-layer deposition techniques and the utilization of ab initio calculations. These competing phases include non-trivial polar textures[9–11], room-temperature magnetoelectric materials[12], improper ferroelectrics[13–15] and antipolar phases[16] resulting from the interplay among strain, electrostatic and gradient energies. There have been efforts to manipulate between these distinct phases with

external stimuli, such as electric fields[17,18], resonant optical excitations[7,8] and strain[19,20]; however, these conversions are often between two non-centrosymmetric states, volatile in nature or irreversible. The ability to both remove and introduce symmetry (and, in particular, polarization) with an electric field in a non-volatile fashion remains elusive, as electric fields generally only break symmetries.

Here we show that this non-volatile interconversion is indeed possible using confined $BiFeO_3$ (BFO) layers as our model system. We stabilized mixed-phase coexistence of a non-centrosymmetric polar and a centrosymmetric antipolar phase by utilizing three design parameters. The first is the discontinuity of the local polarization at the heterointerface. The second is the lattice mismatch arising from the different lattice parameters of the two layers. The third is the discontinuity in the sense and direction of the octahedral rotations in the two layers, which we achieve by using $TbScO_3$ (TSO) as our epitaxial dielectric interleaving layers. The polar and antipolar phases are identified and characterized using a combination of high-resolution and four-dimensional (4D) scanning transmission electron microscopy (STEM), piezoresponse force microscopy (PFM), microwave impedance microscopy (MIM), confocal second harmonic generation (SHG), transport measurements and density-functional theory (DFT). Moreover, using applied electric fields, we interconvert between the polar non-centrosymmetric and antipolar centrosymmetric phases reversibly and in a non-volatile fashion. With this electric-field-driven phase transformation, we show that the applied electric field not only removes centrosymmetry to stabilize polar order, but the electric (that is, polar) field can remarkably re-introduce centrosymmetry and stabilize antipolar order, effectively 'erasing' the polarization in the material. We further demonstrate that electric-field manipulation of the crystal symmetry also manifests as concomitant non-volatile changes in the SHG signal and the d.c. and microwave conductivity. Such large changes in functional materials properties resulting from an electric-field-induced symmetry phase transformation open pathways to opto-electronic devices and highlight a design scheme and materials platform for developing phase-change-based memory and logic.

Coexistence of non-centrosymmetric and centrosymmetric phases

Recent studies have shown that various low-energy phases and polytypes of BFO can be stabilized using different boundary conditions[16,21–25]. The calculated energies and structures of such phases with respect to their unit-cell sizes are shown in Fig. 1a (Methods and Supplementary Fig. 2). Of note is the presence of phases with different crystal symmetries in energetic proximity to the $R3c$ ground state, including a centrosymmetric $Pnma$ phase and large unit-cell non-centrosymmetric Pc phases with polarization waves exhibiting wavelength-dependent relative stability.

The energetic proximity of these BFO phases with different symmetry suggests the possibility of stabilizing multiple coexisting phases with vastly different properties. To investigate this possibility, epitaxial superlattices of $[(BFO)_n/(TSO)_m]_{20}$ for $n = 11$–20, $m = 10$ unit cells were synthesized by reactive molecular-beam epitaxy (MBE) on $GdScO_3$ (GSO) and TSO $[110]_O$ substrates (O denotes orthorhombic orientation; Methods). High-angle annular dark field (HAADF) STEM imaging of a $[(BFO)_{14}/(TSO)_{10}]_{20}$//GSO superlattice shows atomically sharp interfaces, with no obvious presence of crystallographic defects (Fig. 1b and Supplementary Figs. 3 and 4). To study the symmetry of the BFO layers, we used scanning convergent beam electron diffraction (SCBED) coupled with an electron microscopy pixel array detector (EMPAD)[26,27] (Methods). The bright-field image reconstructed from the SCBED dataset (Fig. 1c) reveals the coexistence of two distinct phases within the BFO layers exhibiting bright and dark contrast, respectively. A symmetry analysis (Supplementary Fig. 5) identifies the two phases as the non-centrosymmetric Pc phase (dark regions, Fig. 1c) and a centrosymmetric $Pnma$ phase (bright regions, Fig. 1c).

In polar crystals, the charge redistribution associated with ferroelectric polarization leads to intensity asymmetry in polarity-sensitive Friedel pairs of Bragg reflections in the CBED pattern; hence, SCBED, in combination with dynamical diffraction simulations, enables polarization mapping at subnanometre resolution[28,29] (Supplementary Text 1). Arrows map the polarization from the non-centrosymmetric Pc phase (dark regions in Fig. 1d,c), which shows continuously winding electric dipoles resembling a polarization wave or a series of half-vortices. The continuous rotation of the polarization is represented by $\nabla \times \mathbf{P}$ and is denoted by the blue/red colour overlay (Fig. 1d and Supplementary Fig. 6). The winding dipoles form a net in-plane polarization along the wave direction ($[100]_{pc}$ or $[\bar{1}00]_{pc}$, pc denotes pseudocubic indices) that can vary between and within each BFO layer. The atomic structure of the coexisting centrosymmetric $Pnma$ phase was also probed (Fig. 1e,f and bright regions in Fig. 1c) by HAADF-STEM images along two projections of the crystallographic zone axes (that is, $[100]_{pc}$ and $[010]_{pc}$). Overlaid on these atomic images are the polar-vector maps of the bismuth-ion displacement, which shows the antipolar 'up–up–down–down' order along the $[011]_{pc}$ projection also observed elsewhere[16,22]. The polar and antipolar nature of the two phases is confirmed with charge–voltage hysteresis loops (Supplementary Fig. 7, and see Supplementary Text 2). Therefore, we have stabilized two low-energy phases of BFO with non-centrosymmetric polar and centrosymmetric antipolar properties, where the net polarization of the polarization wave ($[100]_{pc}$ or $[\bar{1}00]_{pc}$) phase orients orthogonally to the local dipoles in the antipolar phase ($<011>_{pc}$). Interestingly, the saturated polarization of both phases, as shown in Supplementary Fig. 7, are similar, suggesting that the high-field state of the antipolar phase is the zero-field phase of the polar phase. HAADF-STEM taken along the $[100]_{pc}$ zone axis reveals the atomically sharp boundary between the coexisting phases (Fig. 1g and Supplementary Fig. 8), suggestive of a diffusion-less, first-order phase transformation[30].

Mixtures of nearly energetically degenerate phases have been the framework used to elicit large responses to external stimuli[31–34]. We demonstrate such large, simultaneous changes in piezoelectricity, optical SHG, microwave response and d.c. conductivity in the mixed-phase superlattices. Lateral PFM phase imaging (Fig. 2a), where contrast is sensitive to in-plane polarization along the $[100]_{pc}$ of the uppermost BFO layer in the sample, reveals distinct, stripe-like regions of high piezoelectric response (white and dark-brown regions) and zero piezoelectric response (orange regions) on the order of several micrometres in width and extending for hundreds of micrometres along the $[010]_{pc}$. Consistent with the HR-STEM vector mapping, the high piezoresponse regions consist of the polar phase of BFO, where white subdomains have net polarization along the $[\bar{1}00]_{pc}$ and dark-brown subdomains have net polarization along the antiparallel $[100]_{pc}$. Regions of zero piezoresponse (orange regions) correspond to the antipolar BFO phase. These observations are confirmed with additional lateral and out-of-plane PFM measurements (Supplementary Fig. 9). The relative stability of each phase can be controlled by tuning the BFO layer thickness in the superlattice. As shown by lateral PFM images (Supplementary Figs. 9 and 10) and confirmed with phase field simulations (Supplementary Fig. 11), small unit-cell changes in the BFO thickness from 11 to 19 unit cells transform the superlattice from a uniform antipolar state[16] to a uniform polar state. Changing the strain state via substrate selection changes the length scales of the domains (Supplementary Fig. 12 and Supplementary Text 3).

Non-linear optical response of mixed-phase coexistence

The coexistence of symmetry-distinct phases also results in a dramatic spatial variation of the non-linear optical response of the material. Unlike PFM, an SHG map (Methods) of a nearby region on the same sample (Fig. 2b) provides information that is integrated throughout
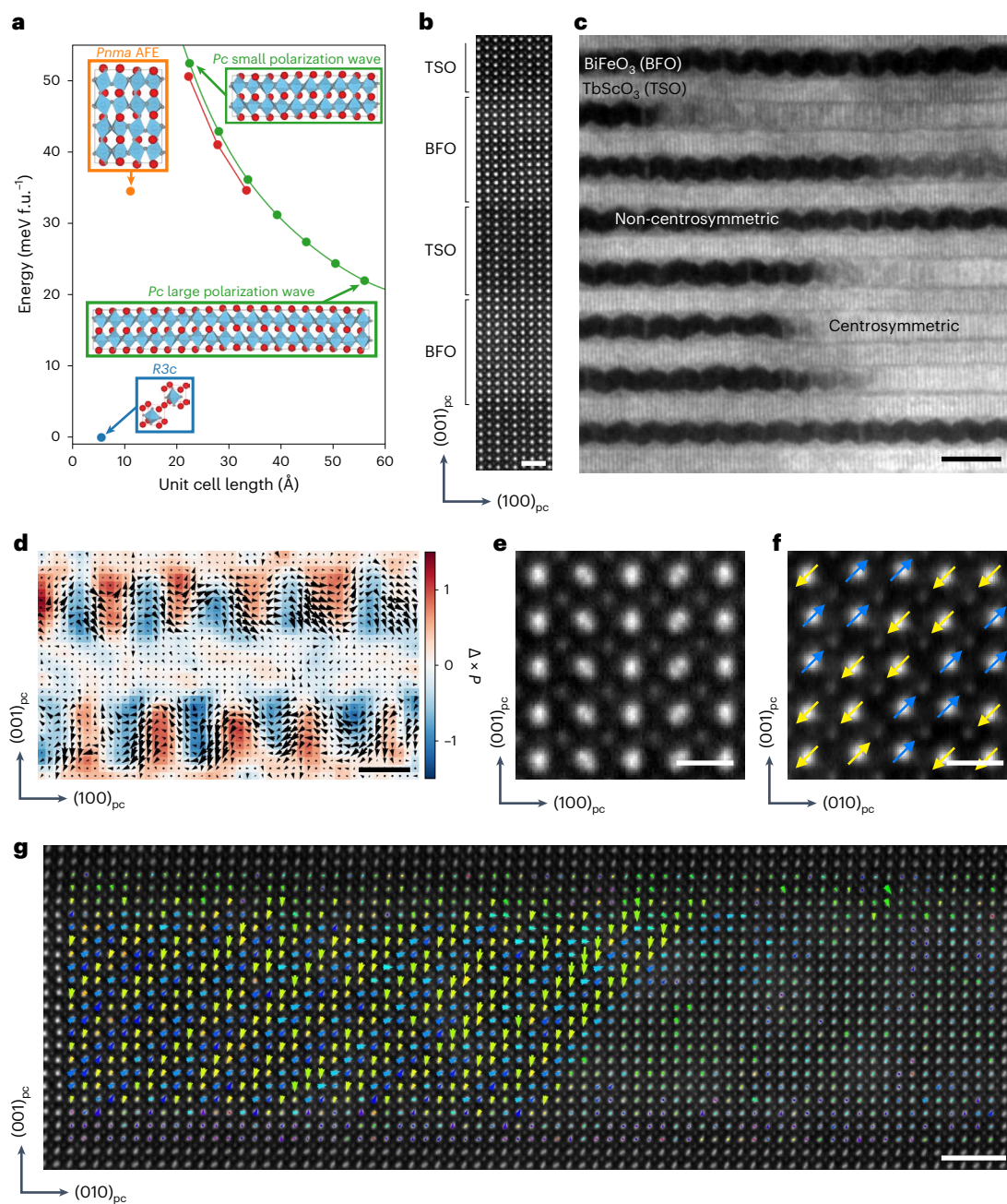
Fig. 1 | Mixed-phase coexistence of polar and antipolar phases in the BFO/TSO superlattice. a, Structures, energies and lattice constants of low-energy phases of BFO with zero out-of-plane net polarization predicted using DFT. AFE, antiferroelectric order parameters; f.u., formula unit. **b**, Atomically resolved HAADF-STEM image of the $[(BFO)_{14}/(TSO)_{10}]_{20}$ superlattice along the $[010]_{pc}$ zone-axis showing atomically sharp interfaces. Scale bar, 10 nm. **c**, Bright-field image obtained from the SCBED dataset showing the spatial distribution of polar (*Pc*) and antipolar (*Pnma*) BFO phases. Scale bar, 10 nm. **d**, Polarization map of the polar phase overlaid with its curl ($\nabla \times \mathbf{P}$) obtained by analysing the Kikuchi bands recorded in the SCBED dataset using an EMPAD. Scale bar, 5 nm. **e,f**, Atomic resolution HAADF-STEM images of the antipolar phase along $[010]_{pc}$ (left) (**e**) and $[100]_{pc}$ (right) (**f**) zone axes. Scale bar, 5 Å. **g**, HAADF-STEM image along $[100]_{pc}$ showing the atomically sharp interface between the antipolar and polar phases. The vectors represent the displacement of Bi atomic columns relative to the four neighbouring Fe columns, showing the 'up–up/down–down' distortion along the $[011]_{pc}$ in the antipolar region. Scale bar, 2 nm.

the thickness of the film[35]. The comparison of PFM and SHG signals helps to distinguish true polarization effects from band-structural changes of the piezoelectric or non-linear optical susceptibilities that may occur upon phase transformation. We select a normal-incidence optical geometry, for which the transversally polarized fundamental and, thus, SHG light probes the in-plane symmetry breaking. Distinct centrosymmetric (dark intensity) and non-centrosymmetric (bright intensity) stripe-like phases of BFO are also seen in Fig. 2b. The distributions of the brightness within the polar regions differ because of SHG

interference occurring at the domain walls (DWs) and the possibility of domains with different polarization directions stacked perpendicular to the film surface. Local SHG polar plots from both phases, in which the incident light polarization is varied and the corresponding vertically (Fig. 2c) or horizontally (Fig. 2d) polarized emitted light at the second harmonic is analysed, are provided. The non-centrosymmetric polar phase (red circles, Fig. 2c,d) shows a two-lobed angle-dependent SHG intensity profile, with two additional minor lobes, consistent with the space group *Pc* (point group *m*) (Fig. 1a) obtained from the CBED
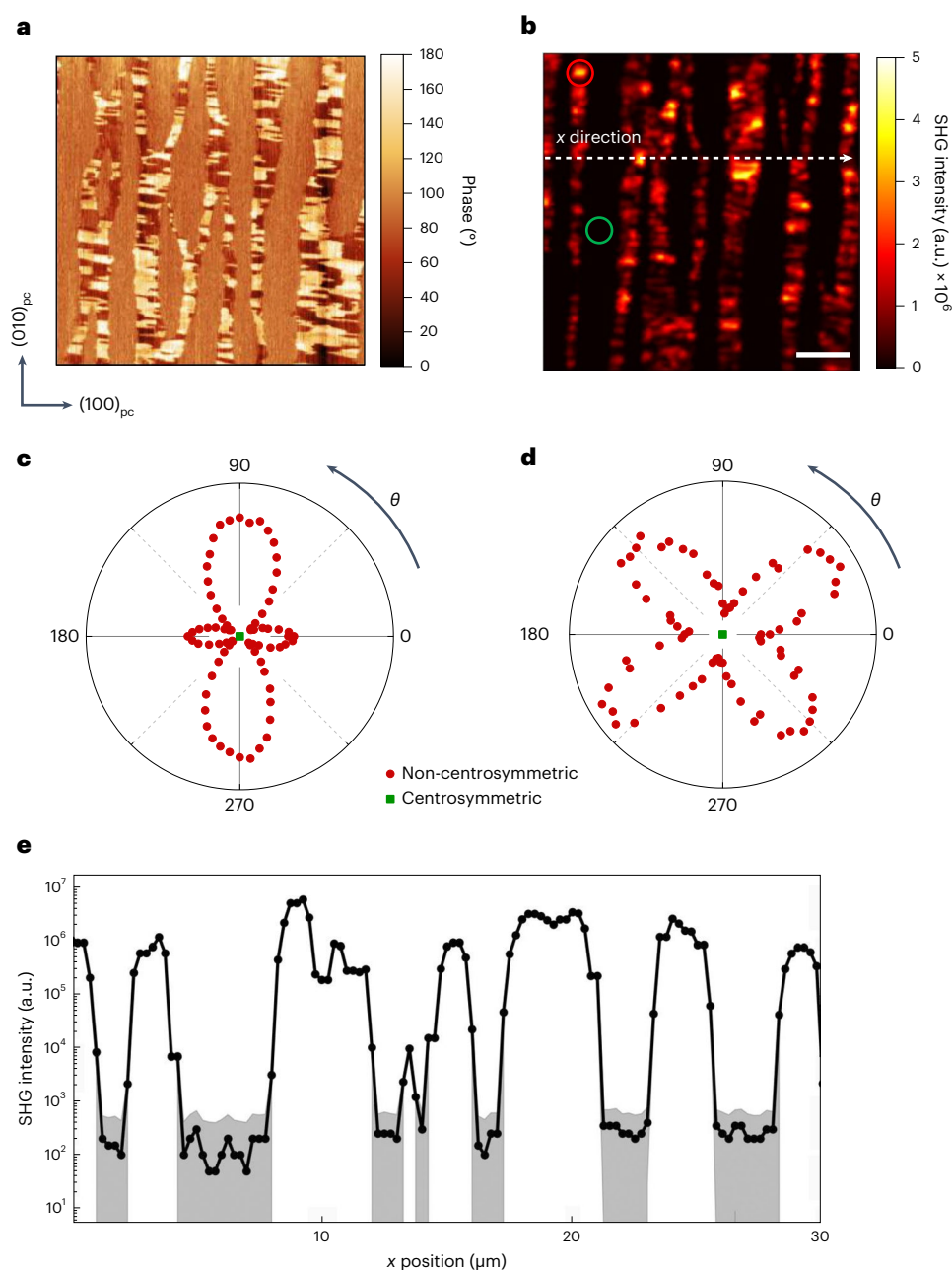
Fig. 2 | Piezoforce and non-linear optical response of mixed-phase coexistence. a, PFM phase image of the $[(BFO)_{14}/(TSO)_{10}]_{20}$ superlattice. Dark regions with near 0° phase angle denote net polarization along the $[100]_{pc}$ direction, as indicated by the white arrow, whereas light regions with near 180° phase denote net polarization along the $[\bar{1}00]_{pc}$ direction, as indicated by the black arrow. Areas exhibiting 90° phase have no net polar order and reflect antipolar regions. **b**, Confocal SHG map on a nearby area of the same sample. Areas showing high (low) SHG intensity contain (non-)centrosymmetric BFO.

c,**d**, Local SHG polar plots from the red and green circled regions in **b**, where the incident light polarization (θ) is varied and the corresponding vertically (**c**) or horizontally (**d**) polarized emitted light at the second harmonic is analysed. Red and green regions correspond to non-centrosymmetric and centrosymmetric phases, respectively. **e**, SHG intensity line profile along the dashed white line in **b**. The uncertainty (grey bands) come from the noise level of the SHG detector. Scale bars, 5 μm. a.u., arbitrary units.

analysis (Supplementary Fig. 5, see SHG selection rules in Methods). On the other hand, the centrosymmetric antipolar phase (green squares, Fig. 2c,d) has no measurable SHG signal regardless of the fundamental or SHG light polarization, consistent with the *Pnma* space group (point group *mmm*) observed in the CBED analysis (Supplementary Fig. 5). Additional PFM phase images and SHG maps are provided (Supplementary Figs. 13 and 14), which scrutinize the spatial correlation of the PFM and SHG signals. The dramatic difference in non-linear optical response from each phase is further highlighted in the line scan (Fig. 2e and dashed white arrow of Fig. 2b), where the SHG intensity is enhanced

by nearly five orders of magnitude in the polar phase relative to the antipolar phase. Consistent with the similar energies of the two phases found in ab initio calculations (Fig. 1a), the piezoelectric, SHG, and CBED data confirm the mixed-phase coexistence of a centrosymmetric antipolar phase and a non-centrosymmetric polar phase.

Dielectric response and conductivity of mixed-phase coexistence

We explore the changes in dielectric permittivity accompanied by such changes in symmetry, which are often observed during phase transitions
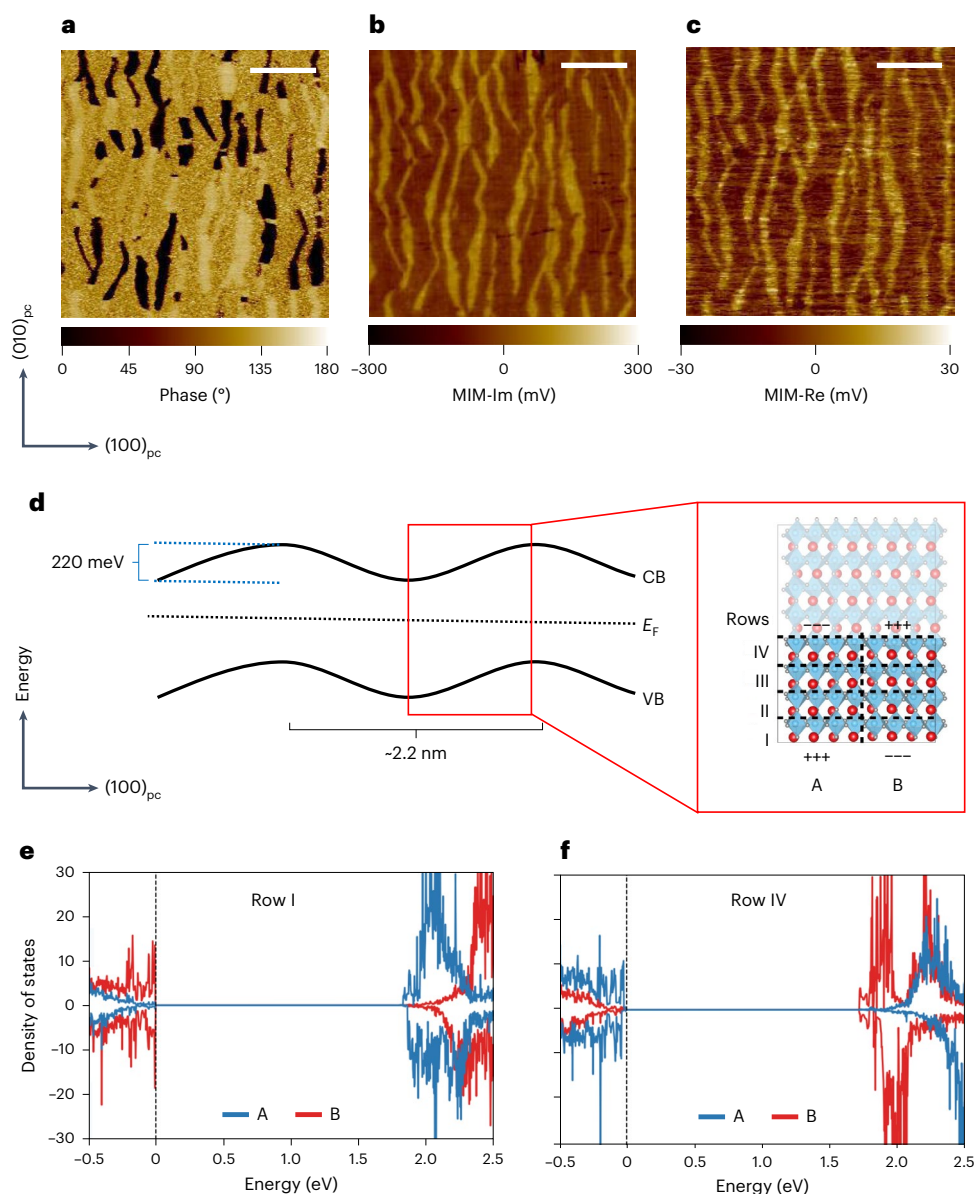
Fig. 3 | MIM and DFT band-structure calculations. a, PFM phase image of a TSO//[(BFO)$_{14}$/(TSO)$_{10}$]$_{20}$ superlattice, where the contrast is sensitive to polarization along the [100]$_{pc}$ direction. **c,b**, Imaginary (Im) (**b**) and real (Re) (**c**) parts of the MIM images taken at the same area as **a**. Scale bars, 2 μm. **d**, Band bending model of the conduction (CB) and valence bands (VB), reducing the effective bandgap of the system by ~0.45 eV. The red enlarged box shows a labelled real-space schematic of the modelled polarization wave. E_F, Fermi energy. DFT-computed density of states for a confined polarization wave heterostructure with 2.2 nm periodicity in **e**, row I and **f**, row IV of regions A and B indicated in **d**, where a built-in voltage is established by the [001]$_{pc}$-oriented component of the wave polarization.

in ferroelectric systems (for example, in temperature-driven phase transitions)[3]. The spatially resolved dielectric response and a.c. conductivity of the superlattices were probed by scanning MIM[36] (Methods). First, by performing PFM with the shielded MIM tip[37], we independently confirmed mixed-phase polar and antipolar coexistence in a separate [(BFO)$_{14}$/(TSO)$_{10}$]$_{20}$ superlattice grown on a TSO substrate (Fig. 3a). We note that, despite the growth of this nominally identical superlattice on a different substrate (that is, strain state), the mixed-phase coexistence is persistent, only manifesting as a difference in domain length scales and not any differences in the nature of the phases formed (also see Supplementary Fig. 12). The imaginary (MIM-Im) and real (MIM-Re) parts of the 2.513 GHz MIM impedance were acquired on the same area as the PFM (Fig. 3c). The one-to-one correlation between the PFM and MIM images is apparent, with the polar phase showing a significantly enhanced signal compared with the antipolar phase, regardless of the polarization direction. We estimated the dielectric contribution

to the MIM-Im contrast by performing finite-element analysis (FEA)[38] of the near-field interaction for the specific tip–sample configuration (Supplementary Fig. 15a,b and Supplementary Text 4), and plotted as a function of the BFO permittivity (Supplementary Fig. 15c). Assuming a dielectric constant $\varepsilon_r \approx 60$ in the polar phase[39], comparing the FEA simulation with the magnitude of the experimentally observed MIM-Im signal (Fig. 3b) yields $\varepsilon_r \approx 30$ for the antipolar phase. This is qualitatively consistent with independent dielectric measurements at low frequencies (Supplementary Fig. 16 and Supplementary Text 5). To determine the conductivity contribution to the MIM contrast, we plot the simulated Re- and Im-MIM signals as a function of sample conductivity[38] (σ; Supplementary Fig. 15d), with the dielectric contribution to the MIM signal accounted for by a vertical shift in the MIM-Im curve relative to the MIM-Re curve. Importantly, the small but measurable contrast in the experimentally observed MIM-Re channel (Fig. 3c) indicates a finite gigahertz conductivity in the polar phase (Supplementary Text 4).
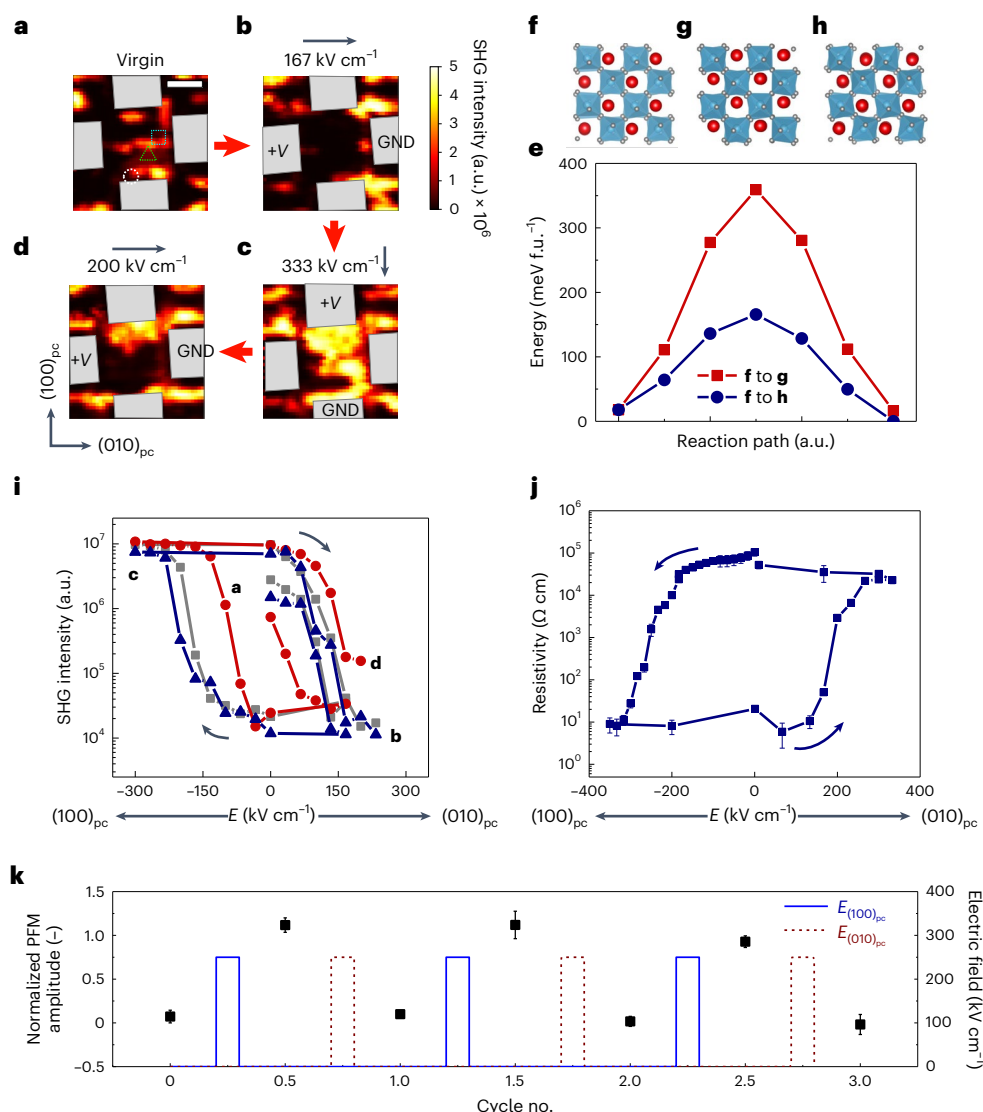
Fig. 4 | Non-volatile electric-field manipulation of SHG intensity and resistivity. a–d, A series of SHG maps under sequentially applied orthogonal in-plane electric fields along the $(010)_{pc}$ (**b**), $(100)_{pc}$ (**c**) and $(010)_{pc}$ (**d**). **a** is the virgin state of the device. Electrodes are denoted by grey overlaid boxes. The magnitude and orientation of the electric field are denoted by arrows and text above each panel and on each electrode. Red arrows between each panel denote the sequence of applied electric field. GND, ground. Scale bar, 3 μm. **e–h**, Energy barriers (**e**) computed by linearly interpolating between polar wave phase **f** and polar wave phase **g** with perpendicular polarization orientations and the antipolar phase (**h**). **i**, An SHG–electric-field hysteresis for the regions outlined in **a**. Each plotted symbol type (circle, square and triangle) corresponds to local hysteresis of the same shape in **a**. The positive and negative horizontal

axes denotes electric field oriented along the $[010]_{pc}$ and $[100]_{pc}$ directions, respectively. The labels **a–d** refer to points along the hysteresis corresponding to panels **a–d**. Data are presented as mean SHG values within each region, and error bars are the SHG detector background noise averaged over 120 s and are smaller than the data points. **j**, Hysteresis of d.c. resistivity with electric field across the top and bottom electrodes in the device. The positive and negative horizontal axis denotes electric field oriented along the $[010]_{pc}$ and $[100]_{pc}$ directions, respectively. Data presented are a mean resistivity value ± standard error over the 120 s measurement. **k**, Normalized PFM amplitude of three electric-field device cycles, with fields alternating along the $[100]_{pc}$ and $[010]_{pc}$ directions between each half cycle as indicated. Data are the average ± standard error of three measurements (Supplemental Fig. 25).

Surprisingly, the simulated σ-dependent MIM contrast (Supplementary Fig. 15d) of the polar phase suggests a conductivity of ~1 S m^{-1} (that is, resistivity of ~100 Ω cm), over the frequency range of 100 MHz to 3 GHz (Supplementary Fig. 15e,f). The width of the grey region denotes the range of σ values within experimental uncertainty. Since this resistivity is approximately five to six orders of magnitude lower than that of bulk BFO, the MIM results suggest that the polar phase displays semiconducting behaviour, whereas the antipolar phase is insulating.

DFT calculations indicate that the bandgaps of the polarization wave and antipolar phases in their hypothetical bulk forms are close to that of the bulk ground-state $R3c$ phase (2.15 eV, Supplementary Fig. 17 and Methods). However, a supercell calculation consisting

of the polarization wave Pc phase alternating between two layers of $Pnma$ BFO phase frozen in their bulk structures yields a significant 0.45 eV reduction in the bandgap of the polarization wave phase to 1.7 eV (Supplementary Fig. 17c,d). The calculated layer-by-layer and wave-polarization-resolved densities of states (Fig. 3d–f and Supplementary Fig. 17e–g) reveal that the effective bandgap reduction originates from alternating band bending caused by the built-in electric fields induced by the local ±$[001]_{pc}$-oriented components of the wave polarization perpendicular to the net polarization of the phase. This large electrostatic reduction in the effective bandgap is responsible for the significant enhancement in conductivity seen in the MIM results (Supplementary Text 6). Moreover, the large bandwidth of conduction

observed in MIM at megahertz and gigahertz frequencies suggests that the conduction is mediated by electrons and not extrinsic effects, such as oxygen vacancy migration. X-ray absorption spectroscopy obtained via spatially resolved photoemission electron microscopy on a mixed-phase superlattice also confirms an Fe^{3+} valence state (Supplementary Fig. 18). Contrary to previous work on one-dimensional conduction observed at ferroelectric DWs[40,41] and phase boundaries[42], the electron conduction observed here occurs through the bulk of the polar phase and does not rely on the presence of defects (DWs and phase boundaries). Moreover, it is isotropic in nature and is a direct manifestation of the confinement of the polarization wave in a superlattice structure.

Electric-field control of centrosymmetry

The phase coexistence and its impact on the physical properties lays the foundation for the study of pathways to interconvert between the two phases with an applied electric field. For this purpose, test structures were fabricated by lithographically patterning a set of orthogonal in-plane electrodes that enable the application of a lateral electric field along both $[100]_{pc}$ and $[010]_{pc}$ (Methods; Supplementary Fig. 19). Using these structures, we measured the field-dependent SHG signal concurrently with in-plane d.c. transport. Starting in the virgin, mixed-phase state (Fig. 4a), upon applying a lateral electric field along the $[010]_{pc}$, we observe the conversion of the polar phase (strong SHG signal) to the antipolar phase (no SHG signal) in a non-volatile fashion (Fig. 4b). We emphasize here that, remarkably, an application of an electric (that is, polar) field along the $[010]_{pc}$ eliminates the net polarization and stabilizes the antipolar state. A similar effect is observed with the application of a negative bias along this direction (that is, along the $[0\bar{1}0]_{pc}$; Supplementary Fig. 14 and Supplementary Text 7). Grey regions within the SHG images denote the lithographically defined electrodes, where the electric-field direction and magnitude are denoted above each SHG panel and overlaid on the electrodes. Applying an electric field along the orthogonal $[100]_{pc}$ (Fig. 4c), the antipolar phase fully reverts back into the polar phase with near uniformity and is non-volatile ($>10^6$ s). Finally, reapplication of an electric field along the $[010]_{pc}$ reforms a near-uniform antipolar state between the electrodes by driving the polar–antipolar phase boundary back in a non-volatile fashion (Fig. 4d), highlighting the complete reversibility of the process, a behaviour that cannot easily be explained by traditionally used order parameter–energy diagrams, but a modified Landau free energy (Supplementary Fig. 1). We note that while coexistence of antipolar and polar phases and electric-field conversion from antipolar to polar states has been reported[43–46], these field-induced phase transitions are typically a volatile saturation of antipolar dipoles along the electric-field direction, relax after relatively short transients and are not a fundamental change of the system's ground state. Here, the non-volatile interconversion between the two phases occurs via a first-order nucleation and growth process, which is illustrated in a sequence of SHG images with finer scale electric-field steps (Supplementary Figs. 20–22 and Supplementary Text 7 and 8), that depicts the motion of the phase boundary and the non-volatility of the symmetry transformation. The non-volatile transformation between the phases is also confirmed with correlative SHG, PFM and MIM imaging (Supplementary Figs. 21 and 23 and Supplementary Text 9) on separate devices, which also demonstrates repeatability. The SHG and PFM data aquisitions occur over several minutes, and the phase transformation kinetics happen within the timescales of our measurement techniques.

These electric-field-dependent switching processes are sensitive to the orientation of the electric field. In other words, an electric field applied parallel to the polarization wave direction ($[100]_{pc}$) results in polar phase stabilization, while an electric field applied perpendicular to this favours the antipolar phase, rather than reorienting the polarization wave. Figure 1a plots the DFT-computed energies for these three scenarios (red and green for the polarization waves

and orange for the antipolar phase). While the relative energy difference between the two polar phases—those with perpendicularly oriented polarization waves—is small and nearly the same as the energy of the antipolar phase, the energy barrier between the polar phases in the two orientations is twice as large as that between the polar phase and the antipolar phase (Fig. 4e), owing to their similar octahedral tilt patterns (Fig. 4f–h). As a result, the antipolar phase is kinetically favoured over the polar phase under a perpendicularly applied electric field. We note that there are two kinds of anisotropy imposed on the system. The first is the anisotropy in octahedral tilts arising from the interweaving TSO layer, and the second is anisotropy arising from the epitaxial strain of the orthorhombic substrates (TSO and GSO). The former affects the switching pathway between polar and antipolar phases, while the latter affects the mesoscale domain formation and their length scales.

Based on the field-dependent imaging of the SHG signal, we record the hysteretic behaviour of the SHG intensity as a function of the applied electric field at given points in the test structure (Fig. 4i; from the locations circled in Fig. 4a), where the positive horizontal axis indicates electric field along the $[010]_{pc}$ and the negative horizontal axis denotes electric field along the $[100]_{pc}$. The SHG intensity is manipulated by approximately three orders of magnitude with full non-volatility (stable $>10^6$ s, Supplementary Fig. 22). While previous efforts have been dedicated to manipulating inversion symmetry of materials probed with electric-field- and current-driven SHG[18,47–51], as well as geometric patterning[52,53], these effects were typically weaker than those observed here and generally arise from manipulation of electronic band structures, in contrast to overtly manipulating crystal symmetry through a phase transition, as is shown here. The field-dependent hysteresis in the SHG data is corroborated by the corresponding hysteretic d.c. transport in Fig. 4j (also see Supplementary Fig. 24), where the d.c. resistivity between the two metal electrodes is modulated by over four orders of magnitude; this is consistent with the range of conductivity observed in each phase in the MIM measurements (Fig. 3) and consistent with an effective bandgap change of ~0.3 eV. The difference in the coercivity between the SHG (Fig. 4i) and resistivity hystereses (Fig. 4j) is directly attributed to the fact that SHG is measured at a single point, whereas the resistivity is a macroscopic manifestation of the connectivity between the metal electrodes. The reliability of the reversible switching process is highlighted in Fig. 4k, where we have poled a device for three successive electric-field cycles and locally measured the PFM response (Supplementary Fig. 25 for PFM images and normalized PFM calculation details). These results are also reproducible across several samples and devices (Supplementary Figs. 9, 15, 21, 23 and 26).

Outlook

Our results show a reversible pathway to convert from one phase to the other with an external electric field, including, remarkably, a mechanism by which an antipolar state can be stabilized with an electric field. Such symmetry and polar order changes are accompanied by dramatic changes in SHG intensity and, more surprisingly, large changes in both the d.c. and microwave conductivity. It is noteworthy that the significant changes in the SHG and transport behaviour, which are a consequence of such a symmetry-distinct phase transition, can enable its use as a mechanism in non-volatile information storage[42], neuromorphic computing[54] and cross-functional devices that take advantage of optical, electronic and ferroic properties of materials.

Online content

Any methods, additional references, Nature Portfolio reporting summaries, source data, extended data, supplementary information, acknowledgements, peer review information; details of author contributions and competing interests; and statements of data and code availability are available at https://doi.org/10.1038/s41563-022-01412-0.

References

1. Robert E Newham. *Properties of Materials: Anisotropy, Symmetry, Structure*. (Oxford Univ. Press, 2004); https://doi.org/10.1093/oso/9780198520757.001.0001

2. Rashba, E. & Sheka, V. Symmetry of energy bands in crystals of wurtzite type II. Symmetry of bands with spin-orbit interaction included. *Fiz. Tverd. Tela Collect. Pap.* **2**, 62–76 (1959).

3. Lines, M. E. & Glass, A. M. *Principles and Applications of Ferroelectrics and Related Materials* (Oxford Univ. Press, 1977); https://doi.org/10.1093/acprof:oso/9780198507789.001.0001

4. Dzyaloshinsky, I. A thermodynamic theory of "weak" ferromagnetism of antiferromagnetics. *J. Phys. Chem. Solids* **4**, 241–255 (1958). & I.

5. Moriya, T. Anisotropic superexchange interaction and weak ferromagnetism. *Phys. Rev.* **120**, 91–98 (1960).

6. Goodenough, J. B. The two components of the crystallographic transition in VO_2. *J. Solid State Chem.* **3**, 490–500 (1971).

7. Li, X. et al. Terahertz field–induced ferroelectricity in quantum paraelectric $SrTiO_3$. *Science* **364**, 1079–1082 (2019).

8. Nova, T. F., Disa, A. S., Fechner, M. & Cavalleri, A. Metastable ferroelectricity in optically strained $SrTiO_3$. *Science* **364**, 1075–1079 (2019).

9. Das, S. et al. Observation of room-temperature polar skyrmions. *Nature* **568**, 368–372 (2019).

10. Yadav, A. K. et al. Observation of polar vortices in oxide superlattices. *Nature* **530**, 198–201 (2016).

11. Jia, C. L., Urban, K. W., Alexe, M., Hesse, D. & Vrejoiu, I. Direct observation of continuous electric dipole rotation in flux-closure domains in ferroelectric $Pb(Zr, Ti)O_3$. *Science* **331**, 1420–1423 (2011).

12. Mundy, J. A. et al. Atomically engineered ferroic layers yield a room-temperature magnetoelectric multiferroic. *Nature* **537**, 523–527 (2016).

13. Bousquet, E. et al. Improper ferroelectricity in perovskite oxide artificial superlattices. *Nature* **452**, 732–736 (2008).

14. Zhao, H. J., Íñiguez, J., Ren, W., Chen, X. M. & Bellaiche, L. Atomistic theory of hybrid improper ferroelectricity in perovskites. *Phys. Rev. B* **89**, 174101 (2014).

15. Diéguez, O., Aguado-Puente, P., Junquera, J. & Íñiguez, J. Domain walls in a perovskite oxide with two primary structural order parameters: first-principles study of $BiFeO_3$. *Phys. Rev. B* **87**, 024102 (2013).

16. Mundy, J. A. et al. Liberating a hidden antiferroelectric phase with interfacial electrostatic engineering. *Sci. Adv.* **8**, eabg5860 (2022).

17. Cherifi, R. O. et al. Electric-field control of magnetic order above room temperature. *Nat. Mater.* **13**, 345–351 (2014).

18. Seyler, K. L. et al. Electrical control of second-harmonic generation in a WSe_2 monolayer transistor. *Nat. Nanotechnol.* **10**, 407–411 (2015).

19. Pouget, J. P., Launois, H., D'Haenens, J. P., Merenda, P. & Rice, T. M. Electron localization induced by uniaxial stress in pure VO_2. *Phys. Rev. Lett.* **35**, 873–875 (1975).

20. Xu, R. et al. Strain-induced room-temperature ferroelectricity in $SrTiO_3$ membranes. *Nat. Commun.* **11**, 3141 (2020).

21. Grosso, B. F. & Spaldin, N. A. Prediction of low-energy phases of $BiFeO_3$ with large unit cells and complex tilts beyond Glazer notation. *Phys. Rev. Mater.* **5**, 054403 (2021).

22. Dong, W. et al. Emergent antipolar phase in $BiFeO_3$-$La_{0.7}Sr_{0.3}MnO_3$ superlattice. *Nano Lett.* **20**, 6045 (2020).

23. Carcan, B. et al. Phase diagram of $BiFeO_3$/$LaFeO_3$ superlattices: antiferroelectric-like state stability arising from strain effects and symmetry mismatch at heterointerfaces. *Adv. Mater. Interfaces* **4**, 1601036 (2017).

24. Prosandeev, S., Wang, D., Ren, W., Íñiguez, J. & Bellaiche, L. Novel nanoscale twinned phases in perovskite oxides. *Adv. Funct. Mater.* **23**, 234–240 (2013).

25. Diéguez, O., González-Vázquez, O. E., Wojdeł, J. C. & Íñiguez, J. First-principles predictions of low-energy phases of multiferroic $BiFeO_3$. *Phys. Rev. B* **83**, 094105 (2011).

26. Tate, M. W. et al. High dynamic range pixel array detector for scanning transmission electron microscopy. *Microsc. Microanal.* **22**, 237–249 (2016).

27. Zuo, J.-M. & Shao, Y.-T. Scanning convergent beam electron diffraction (CBED), the essential questions of why, what and how? *Microsc. Microanal.* **24**, 172–173 (2018).

28. Shao, Y.-T. & Zuo, J.-M. Lattice-rotation vortex at the charged monoclinic domain boundary in a relaxor ferroelectric crystal. *Phys. Rev. Lett.* **118**, 157601 (2017).

29. Tsuda, K., Yasuhara, A. & Tanaka, M. Two-dimensional mapping of polarizations of rhombohedral nanostructures in the tetragonal phase of $BaTiO_3$ by the combined use of the scanning transmission electron microscopy and convergent-beam electron diffraction methods. *Appl. Phys. Lett.* **103**, 082908 (2013).

30. Porter, D. & Easterling, K. E. *Phase Transformations in Metals and Alloys* (Chapman & Hall, 1992).

31. Uehara, M., Mori, S., Chen, C. H. & Cheong, S. W. Percolative phase separation underlies colossal magnetoresistance in mixed-valent manganites. *Nature* **399**, 560–563 (1999).

32. Ahart, M. et al. Origin of morphotropic phase boundaries in ferroelectrics. *Nature* **451**, 545–548 (2008).

33. Yin, Z.-W., Luo, H.-S., Wang, P.-C. & Xu, G.-S. Growth, characterization and properties of relaxor ferroelectric PMN-PT single crystals. *Ferroelectrics* **229**, 207–216 (1999).

34. Damodaran, A. R. et al. Phase coexistence and electric-field control of toroidal order in oxide superlattices. *Nat. Mater.* **16**, 1003–1009 (2017).

35. De Luca, G. et al. Domain wall architecture in tetragonal ferroelectric thin films. *Adv. Mater.* **29**, 1605145 (2017).

36. Chu, Z., Zheng, L. & Lai, K. Microwave microscopy and its applications. *Annu. Rev. Mater. Res.* **50**, 105–130 (2020).

37. Yang, Y. et al. Batch-fabricated cantilever probes with electrical shielding for nanoscale dielectric and conductivity imaging. *J. Micromech. Microeng.* **22**, 115040 (2012).

38. Lai, K., Kundhikanjana, W., Kelly, M. & Shen, Z. X. Modeling and characterization of a cantilever-based near-field scanning microwave impedance microscope. *Rev. Sci. Instrum.* **79**, 063703 (2008).

39. Lu, J. et al. Magnetic susceptibility, phonons and dielectric constant of single crystalline $BiFeO_3$. *J. Phys. Conf. Ser.* **200**, 012106 (2010).

40. Seidel, J. et al. Conduction at domain walls in oxide multiferroics. *Nat. Mater.* **8**, 229–234 (2009).

41. Meier, D. et al. Anisotropic conductance at improper ferroelectric domain walls. *Nat. Mater.* **11**, 284–288 (2012).

42. Edwards, D. et al. Giant resistive switching in mixed phase $BiFeO_3$ via phase population control. *Nanoscale* **10**, 17629–17637 (2018).

43. Dawber, M. et al. Unusual behavior of the ferroelectric polarization in $PbTiO_3$/$SrTiO_3$ superlattices. *Phys. Rev. Lett.* **95**, 177601 (2005).

44. Shirane, G., Sawaguchi, E. & Takagi, Y. Dielectric properties of lead zirconate. *Phys. Rev.* **84**, 476 (1951).

45. Cross, L. E. Antiferroelectric-ferroelectric switching in a simple "kittel" antiferroelectric. *J. Phys. Soc. Japan* **23**, 77–82 (1967).

46. Fthenakis, Z. G. & Ponomareva, I. Intrinsic dynamics of the electric-field-induced phase switching in antiferroelectric $PbZrO_3$ ultrathin films. *Phys. Rev. B* **98**, 054107 (2018).

47. Terhune, R. W., Maker, P. D. & Savage, C. M. Optical harmonic generation in calcite. *Phys. Rev. Lett.* **8**, 404–406 (1962).

48. Cai, W., Vasudev, A. P. & Brongersma, M. L. Electrically controlled nonlinear generation of light with plasmonics. *Science* **333**, 1720–1723 (2011).

49. Kang, L. et al. Electrifying photonic metamaterials for tunable nonlinear optics. *Nat. Commun.* **5**, 5680 (2014).

50. Ruzicka, B. A. et al. Second-harmonic generation induced by electric currents in GaAs. *Phys. Rev. Lett.* **108**, 077403 (2012).

51. Sirtori, C., Capasso, F., Sivco, D. L., Hutchinson, A. L. & Cho, A. Y. Resonant Stark tuning of second-order susceptibility in coupled quantum wells. *Appl. Phys. Lett.* **60**, 151–153 (1998).

52. Nordlander, J., Rossell, M. D., Campanini, M., Fiebig, M. & Trassin, M. Inversion-symmetry engineering in layered oxide thin films. *Nano Lett.* **21**, 2780–2785 (2021).

53. Canfield, B. K. et al. A macroscopic formalism to describe the second-order nonlinear optical response of nanostructures. *J. Opt. A* **8**, S278 (2006).

54. Boyn, S. et al. Learning through ferroelectric domain dynamics in solid-state synapses. *Nat. Commun.* **8**, 14736 (2017).

Publisher's note Springer Nature remains neutral with regard to jurisdictional claims in published maps and institutional affiliations.

[1]Department of Materials Science and Engineering, University of California, Berkeley, CA, USA. [2]School of Applied and Engineering Physics, Cornell University, Ithaca, NY, USA. [3]Department of Physics, University of Texas, Austin, TX, USA. [4]Department of Materials Science and Engineering, Cornell University, Ithaca, NY, USA. [5]Department of Materials, ETH Zurich, Zurich, Switzerland. [6]Department of Materials Science and Engineering, The Pennsylvania State University, University Park, PA, USA. [7]Department of Physics, University of California, Berkeley, CA, USA. [8]State Key Laboratory of Silicon Materials, School of Materials Science and Engineering, Zhejiang University, Hangzhou, China. [9]Hangzhou Global Scientific and Technological Innovation Center, Zhejiang University, Hangzhou, China. [10]Molecular Foundry, Lawrence Berkeley National Laboratory, Berkeley, CA, USA. [11]Leibniz-Institut für Kristallzüchtung, Berlin, Germany. [12]Materials Sciences Division, Lawrence Berkeley National Laboratory, Berkeley, CA, USA. [13]Kavli Institute at Cornell for Nanoscale Science, Ithaca, NY, USA. [14]Present address: School of Engineering, Brown University, Providence, RI, USA. [15]Present address: Mork Family Department of Chemical Engineering and Materials Science, University of Southern California, Los Angeles, CA, USA. [16]These authors contributed equally: Lucas Caretta, Yu-Tsun Shao. ✉e-mail: lucas_caretta@brown.edu; rramesh@berkeley.edu

Methods

MBE

Superlattices of alternating TSO and BFO layers are synthesized by reactive oxide MBE in a Veeco GEN10 MBE with in situ reflection high-energy electron diffraction and X-ray diffraction using distilled ozone as the oxidant species. $(BFO)_m/(TSO)_n$, where n and m refer to the thickness, in unit cells, of the BFO and TSO, respectively, are grown on $(110)_o$ TSO and GSO substrates, where the subscript o denotes orthorhombic indices; note that for TSO and GSO $(110)_o = (001)_{pc}$. The superlattices are grown at a substrate temperature between 650 °C and 680 °C in a background pressure of 5×10^{-6} Torr (mmHg) of distilled O_3 (estimated to be 80% pure O_3). Substrate temperatures are measured by an optical pyrometer with a measurement wavelength of 980 nm focused on a platinum layer deposited on the back side of the substrate.

Electrode patterning and sputter deposition

The device electrodes are a bilayer of Ta(4 nm)/Pt(40 nm), where the Ta metal is used as an adhesion layer. The metals were deposited using d.c. magnetron sputtering (AJA International) at a nominal room temperature with an Ar sputter gas pressure of 2 mTorr and a background base pressure of ~3×10^{-8} Torr. Deposition rates for each element were calibrated using X-ray reflectivity measurements of the film thickness. All electrode devices were patterned using a maskless aligner (Heidelberg Instruments) and standard lift-off processes.

STEM

The plan-view and cross-sectional STEM samples of the $[(BFO)_{14}/TSO)_{10}]$ superlattices were prepared using a FEI Helios focused ion beam with a final milling step of 2 keV to reduce damage. The initial sample surface was protected from ion-beam damage by depositing carbon and platinum layers before milling. HAADF-STEM images were recorded using a Cs-corrected Thermo Fisher Scientific Spectra 300 operated at 300 kV, with a probe semiconvergence angle of 30 mrad and a current of 15 pA.

SCBED for polarization mapping

We performed SCBED experiments using a second-generation electron microscopy pixel array detector (EMPAD-G2). SCBED works by rastering a focused probe in two-dimensional real space (x,y) and collecting a full two-dimensional CBED pattern (k_x, k_y) at each probe position, resulting in a 4D dataset[55,56]. Experimental data was acquired using a FEI Titan operated at 300 keV with 10 pA beam current, 2.45 mrad semiconvergence angle, having a probe of ~8 Å full-width at half-maximum. The CBED patterns were captured by the EMPAD-G2 with exposure time set to 100 μs per frame, for which a 512×512 scan can be recorded in under 2 min. Owing to dynamical diffraction effects, the charge redistribution due to ferroelectric polarization leads to intensity asymmetry in Friedel pairs of Bragg reflections. We use Kikuchi bands as a more robust means to extract polarity information against crystal mis-tilts, which often occur in ferroic oxides because of disinclination strain. By matching with dynamical diffraction simulations, we can unambiguously determine the polarization directions in real space[28,29,57].

Laboratory-based X-ray diffraction

Structural characterization was performed using a Panalytical X'Pert3 MRD 4-circle diffractometer with a Cu source. Two-dimensional reciprocal space maps were measured around the TSO (220) peak.

Ferroelectric characterization

The study of the superlattice domain structures was carried out using an atomic force microscope (MFP-3D, Asylum Research). Dual a.c. resonance tracking PFM was conducted using a conductive Pt-coated probe tip (MikroMasch HQ:NSC18/PT) to image the ferroelectric domain structures using lateral and out-of-plane imaging modes. In-plane hysteresis loops were taken using a Radiant Technologies Precision Multiferroic Tester with a frequency of 100 Hz and an applied voltage

of 150 V on patterned interdigitated electrodes. The lateral resistivity (ρ) is estimated from the two-point resistance (R) measurement shown in Supplementary Fig. 24 via $\rho = RL/A$, where $L = 6$ μm is the distance between two electrodes and A is the cross-sectional area of the sample where the electric field is applied. We approximate that the electric field is uniform throughout the thickness of the sample. The resistance is always measured across the electrodes along the $[100]_{pc}$ direction. However, we note that the results are similar if the resistance is measured across the electrodes along the $[010]_{pc}$. In other words, the resistivity is isotropic.

MIM

The MIM experiments were carried out on a commercial AFM platform (XE-70, Park AFM). The electrically shielded microwave cantilever probes are commercially available from PrimeNano, Inc[37]. The two output channels of MIM correspond to the real and imaginary parts of the local sample admittance, from which the effective a.c. conductivity of the sample can be deduced. Numerical simulation of the MIM signals was performed by the FEA software COMSOL v.4.4. Details of the FEA are included in Supplementary Fig. 15 and Supplementary Text 4.

SHG

SHG measurements were carried out in a normal-incidence reflection geometry. A Ti/sapphire oscillator was used for light excitation with ~100 fs pulses and a centre wavelength of 900 nm, a 78 MHz repetition rate and an average power of <1 mW. To control the polarization of the incoming light, we use a Glan–Thompson polarizer and subsequently send the light through a half-wave plate. The polarized light was then sent through a short-pass dichroic mirror and focused on the sample using an oil immersion objective lens (numerical aperture NA = 1.4). The back-reflected SHG signal was sent through a short-pass filter and detected using a spectrometer (SpectraPro 500i, Princeton Instruments) with a charge-coupled device camera (Peltier-cooled CCD, ProEM+:1600 eXcelon3, Princeton Instruments). A linear polarizer on the back-end optics was used to select emitted light polarization for detection. Diffraction-limited confocal scanning microscopy was used to create SHG intensity maps. A commercial Thorlabs polarimeter was used at the sample location to confirm the incoming light polarization incident on the sample, as well as the light polarization entering the detector. All SHG maps shown throughout the manuscript were performed using $[100]_{pc}$-polarized incident light with no polarizer on the back-end optics. In situ d.c. electric fields are applied to the sample using a Keithley 6430 SUB-FEMTOAMP SourceMeter via a custom, shielded, printed circuit board.

SHG selection rules

We are working with light incident along the direction $z \approx [001]_{pc}$ so that only the x and y components of the SHG susceptibility tensor are addressed. For the polar point group m with $x \approx [100]_{pc}$ (that is, spontaneous polarization along x) this leads to the susceptibilities $\chi_{yyy}, \chi_{yxx}, \chi_{xxy} = \chi_{xyx}, \chi_{xyy}, \chi_{yyxx} = \chi_{yxy}$ that are expected to be non-zero and can be probed by our experiment. These susceptibilities were used to fit the SHG polarity data in Fig. 2c,d. We note that we restrict ourselves to the electric-dipole approach in describing SHG and real values for the susceptibilities.

First-principles calculations

Calculations were performed using DFT[58] with the projector augmented wave method[59] as implemented in the Vienna ab initio simulation package (VASP v.5.4.4)[60]. We used a $12 \times 12 \times 12$ k-point Γ-centred mesh to sample the Brillouin zone corresponding to a five-atom unit cell and chose an energy cutoff of 850 eV for the plane-wave basis. The following valence electron configurations were used: $6s^2 6p^3$ for bismuth, $3d^7 4s^1$ for iron and $2s^2 2p^4$ for oxygen. Note that the inclusion of the $5d^{10}$ electrons in the valence manifold for bismuth and the $3p^6$

for iron were tested for bulk structures and gave similar results. The PBEsol + U functional form of the generalized gradient approximation[61] was used, with a commonly used effective Hubbard-U parameter value of $U_{eff} = 4$ eV for the Fe 3d orbitals[62,63], according to the approach of Dudarev et al.[64]. No ionic relaxation was carried out in the supercell in which the DOS were computed. The energy barrier calculations were performed by interpolating the ionic positions and volumes linearly between the starting and ending structures and relaxing the electronic structure at fixed ionic positions.

Phase field simulations
In the phase field method, the local free energy density is expressed as a function of the local polarization P_i ($i = 1$–3), the local oxygen octahedral tilt order (OTs) θ_i ($i = 1$–3) and antiferroelectric order parameters (AFEs) q_i ($i = 1$–3). The total free energy of a mesoscale domain structure described by the spatial distribution of polarization, oxygen octahedral tilt and antiferroelectric order is then the volume integration of bulk free energy density, elastic energy density, electrostatic energy density and gradient energy density,

$$F = \int \Big[\alpha_{ij}P_iP_j + \alpha_{ijkl}P_iP_jP_kP_l + \alpha_{ijklmn}P_iP_jP_kP_lP_mP_n + \beta_{ij}\theta_i\theta_j$$
$$+\beta_{ijkl}\theta_i\theta_j\theta_k\theta_l + \gamma_{ij}q_iq_j + \gamma_{ijkl}q_iq_jq_kq_l + \gamma_{ijklmn}q_iq_jq_kq_lq_mq_n$$
$$+t_{ijkl}P_iP_jq_kq_l + f_{ijkl}P_iP_j\theta_k\theta_l + h_{ijkl}q_iq_j\theta_k\theta_l + \tfrac{1}{2}g_{ijkl}P_{i,j}P_{k,l}$$
$$+\tfrac{1}{2}k_{ijkl}\theta_{i,j}\theta_{k,l} + \tfrac{1}{2}m_{ijkl}q_{i,j}q_{k,l} + \tfrac{1}{2}c_{ijkl}\left(\varepsilon_{ij} - \varepsilon_{ij}^0\right)\left(\varepsilon_{kl} - \varepsilon_{kl}^0\right)$$
$$-E_iP_i - \tfrac{1}{2}\varepsilon_b\varepsilon_0E_iE_j \Big]dV,$$

where α_{ij}, α_{ijkl}, α_{ijklmn}, β_{ij}, β_{ijkl}, γ_{ij}, γ_{ijkl}, γ_{ijklmn}, t_{ijkl}, f_{ijkl} and h_{ijkl} are local potential coefficients representing the stiffness with respect to the changes in the polarization, oxygen octahedral tilt and antiferroelectric order. g_{ijkl}, k_{ijkl} and m_{ijkl} are the gradient energy coefficients of polarization, OTs and AFEs, respectively. ε_b is the isotropic background dielectric constant and ε_0 is the dielectric constant of free space. The eigenstrain ε^0 is coupled to the polarization, AFEs and OTs through $\varepsilon_{ij}^0 = Q_{ijkl}P_iP_l + N_{ijkl}q_iq_l + L_{ijkl}\theta_i\theta_j$, where Q_{ijkl}, N_{ijkl} and L_{ijkl} are the coupling coefficients.

The temporal and spatial evolution of the polarization, OTs and AFEs are governed by the relaxation equations leading to the minimization of the total free energy of the system. In the simulations, periodic boundary conditions are used along three dimensions. For the mechanical boundary condition, the in-plane directions are clamped while the out-of-plane direction is assumed to be stress-free. A pseudo-two-dimensional mesh of $300 \times 2 \times N$ is used, where N indicates the film thickness and the grid spacing is 0.4 nm. The value of N ranges from 60 to 345 based on different simulation conditions. Paraelectric insulating layers are simulated with different dielectric constants. All simulations are performed for a temperature of 300 K.

Data availability
Data presented in the main text are open access and can be found on Zenodo[65] or as Source data accompanying this manuscript. Owing to the extent of data presented in the Supplementary Information, it is available upon request from the corresponding authors.

References
55. Zuo, J. M. & Spence, J. C. H. *Advanced Transmission Electron Microscopy: Imaging and Diffraction in Nanoscience* (Springer, 2016); https://doi.org/10.1007/978-1-4939-6607-3
56. Ophus, C. Four-dimensional scanning transmission electron microscopy (4D-STEM): from scanning nanodiffraction to ptychography and beyond. *Microsc. Microanal.* **25**, 563–582 (2019).
57. Müller-Caspary, K. et al. Electrical polarization in AlN/GaN nanodisks measured by momentum-resolved 4D scanning transmission electron microscopy. *Phys. Rev. Lett.* **122**, 106102 (2019).
58. Kohn, W. & Sham, L. J. Self-consistent equations including exchange and correlation effects. *Phys. Rev.* **140**, A1133 (1965).
59. Blöchl, P. E. Projector augmented-wave method. *Phys. Rev. B* **50**, 17953 (1994).
60. Kresse, G. & Furthmüller, J. Efficient iterative schemes for ab initio total-energy calculations using a plane-wave basis set. *Phys. Rev. B* **54**, 11169 (1996).
61. Perdew, J. P., Burke, K. & Ernzerhof, M. Generalized gradient approximation made simple. *Phys. Rev. Lett.* **77**, 3865 (1996).
62. Neaton, J. B., Ederer, C., Waghmare, U. V., Spaldin, N. A. & Rabe, K. M. First-principles study of spontaneous polarization in multiferroic BiFeO$_3$. *Phys. Rev. B* **71**, 014113 (2005).
63. Shenton, J. K., Bowler, D. R. & Cheah, W. L. Effects of the Hubbard U on density functional-based predictions of BiFeO$_3$ properties. *J. Phys. Condens. Matter* **29**, 445501 (2017).
64. Dudarev, S. L., Botton, G. A., Savrasov, S. Y., Humphreys, C. J. & Sutton, A. P. Electron-energy-loss spectra and the structural stability of nickel oxide: an LSDA+U study. *Phys. Rev. B* **57**, 1505–1509 (1998).
65. Caretta, L. et al. Nonvolatile electric field control of inversion symmetry: manuscript data. *Zenodo* https://doi.org/10.5281/zenodo.7130638 (2022).

Acknowledgements

Author contributions
R.R., D.G.S., L.C. and A.B.M. conceived the project and planned the experiments. Y.-T.S. and H.K.P. performed TEM, TEM sample preparation and atomically resolved polar and structural analysis under supervision of D.A.M. A.B.M. optimized synthesis of the superlattices and performed reciprocal space maps under supervision of D.G.S. L.C. and P.B. performed in-situ SHG measurements with help from A.R. and E.B., and M.F. L.C., P.B. and E.B. prepared the

Competing interests

Additional information